OPEN ACCESS



Limits on Leptonic TeV Emission from the Cygnus Cocoon with Swift-XRT

David Guevel¹, Andrew Beardmore², Kim L. Page², Amy Lien³, Ke Fang¹, Luigi Tibaldo⁴, Sabrina Casanova⁵, and Petra Huentemeyer⁶

Department of Physics, Wisconsin IceCube Particle Astrophysics Center, University of Wisconsin, Madison, WI, USA; guevel@wisc.edu
School of Physics & Astronomy, University of Leicester, University Road, Leicester LE1 7RH, UK
University of Tampa, 401 W Kennedy Blvd, Tampa, FL, USA

⁴ IRAP, Université de Toulouse, CNRS, CNES, UPS, 9 avenue Colonel Roche, F-31028 Toulouse, Cedex 4, France ⁵ Institute of Nuclear Physics Polish Academy of Sciences, PL-31342 IFJ-PAN, Krakow, Poland ⁶ Department of Physics, Michigan Technological University, Houghton, MI, USA Received 2022 November 16; revised 2023 April 5; accepted 2023 April 16; published 2023 June 15

Abstract

 γ -ray observations of the Cygnus Cocoon, an extended source surrounding the Cygnus X star-forming region, suggest the presence of a cosmic-ray accelerator reaching energies up to a few PeV. The very-high-energy (VHE; 0.1–100 TeV) γ -ray emission may be explained by the interaction of cosmic-ray hadrons with matter inside the Cocoon, but an origin of inverse Compton radiation by relativistic electrons cannot be ruled out. Inverse Compton γ -rays at VHE are accompanied by synchrotron radiation peaked in X-rays. Hence, X-ray observations may probe the electron population and magnetic field of the source. We observed 11 fields in or near the Cygnus Cocoon with the Neil Gehrels Swift Observatory's X-Ray Telescope (Swift-XRT) totaling 110 ks. We fit the fields to a Galactic and extragalactic background model and performed a log-likelihood ratio test for an additional diffuse component. We found no significant additional emission and established upper limits in each field. By assuming that the X-ray intensity traces the TeV intensity and follows a $dN/dE \propto E^{-2.5}$ spectrum, we obtained a 90% upper limit of $F_X < 8.7 \times 10^{-11} \, \mathrm{erg \, cm^{-2} \, s^{-1}}$ or $< 5.2 \times 10^{-11} \, \mathrm{erg \, cm^{-2} \, s^{-1}}$ on the X-ray flux of the entire Cygnus Cocoon between 2 and 10 keV depending on the choice of hydrogen column density model for the absorption. The obtained upper limits suggest that no more than one-quarter of the γ -ray flux at 1 TeV is produced by inverse Compton scattering, when assuming an equipartition magnetic field of $\sim 20 \, \mu G$.

Unified Astronomy Thesaurus concepts: Gamma-ray sources (633); X-ray sources (1822)

1. Introduction

The cosmic-ray spectral energy distribution features a spectral break, commonly called "the knee," at a few PeV. The knee is believed to mark the transition from Galactic to extragalactic cosmic-ray origin. The accelerators that produce the highest-energy Galactic cosmic rays, known as PeVatrons, have not been conclusively identified. The Cygnus Cocoon, from which γ -rays above 100 TeV have been detected (Abeysekara et al. 2021; Cao et al. 2021; Tibet AS γ Collaboration et al. 2021), is a prime PeVatron candidate. The Cygnus Cocoon contains the Cyg OB2 stellar association and NGC 6910 stellar cluster, as well as the γ -Cygni supernova remnant but extends beyond them. The winds of massive stellar clusters inside the Cocoon may potentially accelerate particles to PeV energies (Morlino et al. 2021; Vieu et al. 2022a, 2022b).

GeV and TeV γ -rays have been seen by the Fermi Large Area Telescope (LAT; Atwood et al. 2009) up to 100 GeV (Ackermann et al. 2011), the High Altitude Water Cherenkov Observatory (HAWC; Abeysekara et al. 2013) beyond 100 TeV (Abeysekara et al. 2021), and by the Large High Altitude Air Shower Observatory (LHAASO) up to 1.4 PeV (Cao et al. 2021). The Fermi-LAT analysis by Ackermann et al. (2011) did not make it possible to distinguish hadronic and leptonic emission mechanisms. If the emission has a purely hadronic

Original content from this work may be used under the terms of the Creative Commons Attribution 4.0 licence. Any further distribution of this work must maintain attribution to the author(s) and the title of the work, journal citation and DOI.

origin, the cosmic-ray spectrum must be \sim 1.6 times the local proton and helium cosmic-ray spectrum at 10 GeV. The cosmic rays must also have a harder spectrum, suggesting that they are younger than the local cosmic rays. The amplification factor implies a volume energy density 50% higher than the local value. If the emission is purely leptonic, the electron spectrum must be enhanced by a factor of 60 at 10 GeV relative to the local electron spectrum and must also have a harder spectrum (Abeysekara et al. 2021). Further analysis of the Fermi-LAT data (Astiasarain et al. 2023) identified multiple components to the Cocoon emission including an extended component with a broken power-law spectrum and a central component with a hard power-law spectrum. These components can be modeled by diffusion of either hadronic or leptonic particles. The HAWC Collaboration found a change in the spectral shape at around 1 TeV and suggests that the morphology and spectral shape are consistent with proton interaction, though a leptonic contribution cannot be ruled out (Abeysekara et al. 2021).

The electron population that inverse Compton scatters will necessarily produce synchrotron X-rays in the presence of a magnetic field. The Klein Nishina effect suppresses inverse Compton scattering for optical and UV photons so that the TeV emission mostly traces the diffuse dust radiation field rather than the stellar radiation field. An X-ray counterpart to the Cocoon will trace the extended TeV emission if some of the TeV emission is in fact produced by inverse Compton scattering.

Mizuno et al. (2015) used Suzaku to constrain the X-ray 2–10 keV intensity from the Cocoon to less than $2.35 \times 10^{-8} \, \mathrm{erg \ cm^{-2} \ s^{-1} \ sr^{-1}}$ based on two on-source

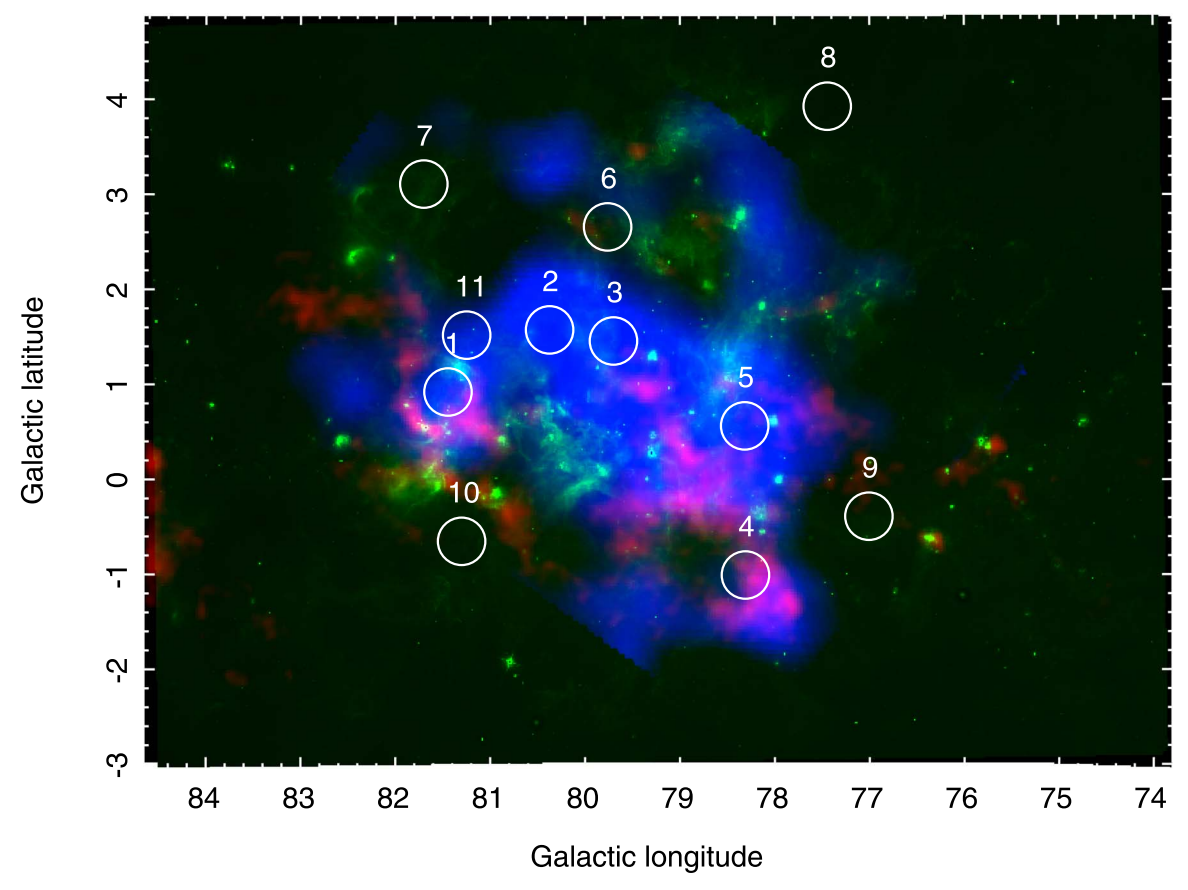


Figure 1. Multiwavelength map of the Cygnus Cocoon. Red is the Planck CO map (Planck Collaboration et al. 2014), green is a WISE 12 micron mosaic (Wright et al. 2010), and blue is the HAWC significance map above 1 TeV using 1343 days of HAWC data (Abeysekara et al. 2021). The blue cutoff approximately corresponds to 3σ . White circles indicate the 11 fields observed by Swift-XRT and analyzed in this work.

observations pointing at strong GeV emission and two off-source observations. The Suzaku 2–10 keV intensity decreases monotonically with Galactic latitude, but the brightest source is actually labeled as one of their background targets (BG1). The 2–10 keV upper limits are calculated by taking the two onsource observations (Source1 and Source2) and subtracting the fainter of the two backgrounds (BG2). The Suzaku off-source regions are actually within the TeV emitting region found by HAWC, which was not known at the time, so they may include some Cocoon emission. The upper limit on X-ray flux from the entire Cocoon is found by extrapolating the upper-limit intensity to the size of the Cocoon (4.38×10^{-3} sr), finding an upper-limit flux density of 6.41×10^{-11} erg cm⁻² s⁻¹ at 1 keV assuming a spectral index equal to 2.

We observed eleven fields within and around the TeV emission of the Cygnus Cocoon found by HAWC with the Neil Gehrels Swift Observatory's X-Ray Telescope (Swift-XRT) to search for evidence of leptonic emission. We establish $2-10 \, \mathrm{keV}$ upper limits on the intrinsic (unabsorbed) Cocoon intensity in seven fields assuming an $E^{-2.5}$ spectrum as suggested by the leptonic model by Abeysekara et al. (2021). Additionally, we derive upper limits on the solid angle integrated Cocoon emission assuming that the X-ray emission traces the TeV emission.

We describe our observations and data processing in Section 2. Our spectral fitting is described in Section 3. We discuss the implications for the leptonic TeV emission in Section 4.

2. Observations and Data Processing

2.1. Observations

Swift observed 10 fields in or near the Cygnus Cocoon from 2021 May 27 to 2021 December 19, and one additional field as a target of opportunity from 2022 May 4 to 2022 June 13. Each field was observed for approximately 10 ks. Seven targets (labeled 1–6, 11) are within the TeV emitting region and four (labeled 7–10) surround the Cocoon to provide a reference for the X-ray background. The fields are shown in Figure 1 with infrared, radio, and TeV observations of the Cocoon and summarized in Table 1.

2.2. Data Processing

We retrieved event lists and exposure maps from the HEASARC (Nasa High Energy Astrophysics Science Archive Research Center (Heasarc) 2014). Each field was observed multiple times, so we produced an image by combining each of the event lists using XSelect. We ran a point-source detection algorithm in XImage to search for point sources with signal-to-noise greater than 3. For each point source found, we excluded a circle with 30" radius around it from further processing. We also excluded detector regions affected by stray light (see Section 2.3). Fields 2, 3, and 9 were affected by stray light from nearby X-ray sources. After stray-light removal, Field 9 had too few counts to provide a useful constraint so we do not use it in the following analysis. We extract a spectrum from the entire remaining detector after point-source and stray-light filtering.

Table 1Summary of Observations

Field	Target ID	1 (deg)	b (deg)	Exposure (s)	$\frac{F_{\gamma,n}}{F_{\gamma,1}}$	
1	95932	81.418	+0.921	10007	1.00	
2*	95933	80.341	+1.597	9817	1.23	
3*	95934	79.714	+1.510	8256	1.28	
4	95935	78.295	-0.975	8309	0.71	
5	95936	78.327	+0.586	9282	1.11	
6	95937	79.710	+2.684	9610	0.46	
7^{\dagger}	95938	81.683	+3.110	9025	0.24	
8^{\dagger}	95939	77.457	+3.945	7554	_	
9*†	95940	76.973	-0.402	9012	_	
10^{\dagger}	95941	81.297	-0.622	7994	_	
11	15110	81.246	+1.521	10723	0.91	

Note. Dagger (†) indicates that the field is outside of the Cocoon and used as background. Star (*) indicates a field that is contaminated by stray light. The treatment of stray light contamination is discussed in Section 2.3. The ratio of TeV γ -ray emission in each field relative to Field 1 (rightmost column) is used in Section 3.5. TeV data were not available for the background fields 8, 9, and 10, which are outside the Cocoon.

We produced an exposure map for each field by summing the individual exposure maps. We produced calibration files using the XRT tools with the extended source option enabled in the XRT xrtmkarf task.

2.3. Stray-light Filtering

Swift-XRT observations can be contaminated by stray light from X-ray sources outside the telescope field of view (Moretti et al. 2009). Because we are searching for a source which is extracted from the entire detector, stray-light contamination can strongly affect the spectrum. In unprocessed images of Fields 2, 3, and 9, the stray light appears in a characteristic ring-like pattern. The centers of Fields 2 and 3 are approximately 45' from Cyg X-3, which is likely the source of the stray light that contaminates up to half of the detector for those observations. The stray light in those fields is temporally variable with a hard power-law spectrum consistent with a high-mass X-ray binary like Cyg X-3. The source of stray light in Field 9 is unknown, but it features a similar hard power-law spectrum, suggesting another X-ray binary. We excluded contaminated detector regions in Fields 2 (54% detector area excluded) and 3 (43% detector area excluded), and produced spectra from the remaining detector area. Stray-light filtering removed 79% and 81% of the events recorded in Fields 2 and 3. Field 9 had 62% of its area excluded and only 15% of the counts remained after filtering. After filtering, there were too few counts remaining to provide a useful constraint in Field 9. There are 10 observations with useful data (1-8, 10, 11). Below, "all fields" refers to fields 1-8, 10, and 11.

3. Spectral Fitting

3.1. Modeling

We include four components in the astrophysical background model: the Galactic ridge X-ray background (GRXB), the local hot bubble (LHB), cosmic X-ray background (CXB), and the solar wind charge exchange (SWCX). The model for the Cocoon is an absorbed power law. The model components are summarized below:

- 1. *GRXB*. The GRXB is an apparent diffuse X-ray emission along the Galactic plane (Ebisawa et al. 2005; Revnivtsev et al. 2006). Previous studies have found that a two-temperature model is necessary to explain X-ray observations of the Galactic plane. We model the GRXB with two absorbed Astrophysical Plasma Emission Code (APEC; Smith et al. 2001; Foster et al. 2012) plasmas following previous studies of the GRXB (Koyama et al. 1986; Mizuno et al. 2015). We refer to these as the "hot" and "cold" GRXB. Both components are absorbed by the tbabs or tbgrain component. The column density of the cold GRXB is allowed to float in the fits while the hot GRXB absorption column density is frozen to the Galactic value (see Section 3.2).
- LHB. The local hot bubble is an apparent cavity of low-density unabsorbed plasma that contains the solar system (Snowden et al. 1997; Kuntz & Snowden 2008; Liu et al. 2016). We model the LHB by an unabsorbed APEC plasma, which dominates the spectra below 0.5 keV.
- 3. CXB. The cosmic X-ray background is a diffuse, isotropic background originating from unresolved active galactic nuclei (Moretti et al. 2003). The CXB is modeled by an absorbed power law with normalization and spectral index frozen to the results of Moretti et al. (2009). The absorption column density is frozen to the Galactic column density.
- 4. SWCX. The solar wind charge exchange is X-ray line emission caused by charge transfer between solar wind ions and neutral atoms (Snowden et al. 2004; Kuntz 2019). We model the SWCX with a single line at 0.5 keV. In reality, the SWCX features many lines, but the Swift-XRT energy resolution at low energy is broad enough that the single line is adequate.
- 5. Cocoon. A hypothetical Cocoon component is modeled by an absorbed power law. Over the fit range 0.3–6.0 keV, a power law adequately represents the expected synchrotron emission. The spectral index was frozen to 2.5 motivated by the HAWC TeV result and the neutral hydrogen column density was frozen to the nearby column density (see Section 3.2). We also tested a spectral index of 2.0.

We include a non-X-ray background spectrum using data collected while the Swift-XRT Sun shutter closed. We use 43 ks of data starting from 2007 September 5 01:30:42 UT when an improper slew caused the Sun shutter to close automatically when the spacecraft slewed within 15° of the Sun (Moretti et al. 2009). XRT continued to collect data with the Sun shutter closed. This spectrum and its response is included in XSpec as a background for all the spectra. The non-X-ray background rate is approximately 2×10^{-8} counts s⁻¹ keV⁻¹ pixel⁻¹. Each of the observations include up to 38,000 pixels (with 2".36 pixel scale), which equates to a background rate 0.007 counts s⁻¹ keV⁻¹. The spectra are dominated by non-X-ray background above 6 keV. A fit for one field is shown in Figure 2.

3.2. N_H Column Density

The choice of column density, particularly the column density of nearby gas absorbing emission from the Cygnus region, affects the upper limit of the intrinsic emission from the Cocoon. To quantify this impact, we estimated the column density two ways. First, we estimate the absorption column

Figure 2. Spectrum from Field 11. The data are shown with error bars overlaid with the overall model (black line). The model components are the solar wind charge exchange (SWCX; pink triple-dotted–dashed), local hot bubble (LHB; red solid), cold Galactic ridge X-ray background (GRXB; green dash), hot GRXB (cyan dot), and cosmic X-ray background (CXB; blue dotted–dashed). The non-X-ray background is plotted with error bars (black crosses) and dominates above 6 keV.

densities from three-dimensional dust maps by Green et al. (2019) using the dustmaps software package (Green 2018). We extract the reddening, E(g - r), at 1.4 and 10 kpc for each of our fields and convert it to E(B-V). We convert E(B-V)to the neutral hydrogen column density using the relation from Valencic & Smith (2015). Second, we use the column density maps derived by Ackermann et al. (2012). The latter uses the Doppler shift of the 21 cm and CO emission lines to kinematically separate H_I and H₂ into two regions: the Local Arm (where the Cygnus region and Cocoon are embedded), and beyond. Additional visual extinction suggests additional dark neutral gas, which was assumed to be molecular gas in the Local Arm. The conversion between CO emission and visual extinction to column density is based on γ -ray data. The column densities are compared in Figure 3. The average nearby kinematic separation column density is 2.1 times higher than the dust map result, and the average total Galactic column density is 1.4 times larger suggesting larger attenuation within the Cocoon. Wilms et al. (2000) suggest an H_2 fraction of 20%, which is assumed in the tbabs model; however, the kinematic separation finds that the average fraction of hydrogen atoms in the molecular phase is approximately 50% for this region.

3.3. Hypothesis Testing

We performed a log-likelihood ratio test (LRT) for the models in the following sections where the null hypothesis is that there is no additional diffuse component and the test hypothesis is that there is additional emission as described in item 5 in Section 3.1. Each model was fit by minimizing the C-statistic (equivalently maximizing the Poisson likelihood) with XSpec (Cash 1979; Arnaud 1996) between 0.3 and 6.0 keV. The models are nested, but the fit parameter space is constrained to keep the Cocoon normalization positive or zero. The test statistic (twice the log-likelihood ratio) thus follows a " $\chi^2/2$ " distribution: CDF(TS) = $1/2 + \int_0^{TS} dx \chi^2(x)/2$ for TS > 0 (Mattox et al. 1996; Protassov et al. 2002). We verified

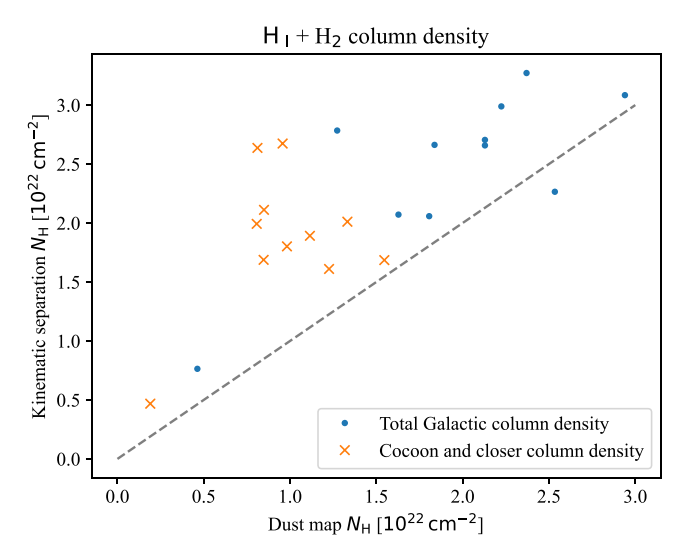


Figure 3. Atomic and molecular hydrogen column densities derived from visual extinction of stars and kinematic separation of 21 cm and CO lines combined with γ -ray data. The gray dashed line would be a perfect correspondence.

that the test statistic does follow this distribution using Monte Carlo simulations where we generated synthetic data sets based on the best-fit background model and performed a likelihood ratio test on each data set. The resulting test statistic distribution had a $\chi^2/2$ distribution with half the trials having TS = 0. Intuitively, the unconstrained Cocoon normalization would be normally distributed around zero. In the constrained case, the negative values are forced to be zero and thus have test statistic equal to zero. For significance lower than 3σ , upper limits for the parameters are defined by the 90% confidence upper confidence interval on the parameter fit.

3.4. Individual Fields

We fit each field with a background and a Cocoon plus background model. The plasma temperatures, normalizations, and absorption column densities are allowed to vary in both fits. In the latter case, the normalization of the Cocoon component is allowed to vary. The best-fit parameters for the background-only model are tabulated in Table 2. In general, the temperatures are similar except where the fit is poorly constrained by limited statistics at higher energy. The background fields (7-10) in particular poorly constrain the hot GRXB. The 2-10 keV intensity after subtracting CXB for each field is shown in Figure 4. Unlike Mizuno et al. (2015), we find no monotonic relationship between the intensity and Galactic latitude. Our Field 3 nearly overlaps the Suzaku Src 1 field and we find similar intensity in these two fields above 2 keV. Field 3 and 6 are the nearest to Suzaku Src 2 but are 48' and 65' away. The hard band intensity in Src 2 is similar to the intensity in Field 6. We performed the hypothesis test described in Section 3.3 for an additional Cocoon component in the onsource fields modeled by an absorbed power law. No field has a Cocoon component with significance greater than 3σ . The 90% confidence upper limits on the Cocoon power-law normalization are shown in Table 2. The mean upper limit is $2.0 \times 10^{-8} \,\mathrm{erg} \,\mathrm{cm}^{-2} \,\mathrm{s}^{-1} \,\mathrm{sr}^{-1}$ between 2 and 10 keV.

Guevel et al.

 Table 2

 Summary of Individual Background-only Fit Results and Upper Limits

Field	C- statistic	DoF	SWCX			LHB		Cold GRXB		Hot GRXB			Cocoon			
			Energy	norm	kT	norm*	$N_{ m H}$	kT	norm*	$N_{ m H}$	kT	norm*	N _H	Spectral Index	000000000000000000000000000000000000	$2 - 10 \text{ keV}$ Intensity $\times 10^{-8} \text{ erg}$
			keV	$\times 10^{-4} \text{ cm}^{-2} \text{ s}^{-1}$	$\times 10^{-2} \text{ keV}$	$\times 10^{-3}$	$\times 10^{22}~\rm cm^{-2}$	keV	$\times 10^{-3}$	$\times 10^{22}~\rm cm^{-2}$	keV	$\times 10^{-3}$	$\times 10^{22}~\mathrm{cm}^{-2}$		keV^{-1}	${\rm cm}^{-2}~{\rm s}^{-1}~{\rm sr}^{-1}$
1	464.96	479	$0.69^{+0.05}_{-0.05}$	$1.03^{+0.52}_{-0.50}$	$7.26^{+0.79}_{-0.75}$	19.86 ^{+15.33} _{-7.52}	$1.33^{+0.18}_{-0.20}$	$0.56^{+0.09}_{-0.13}$	9.81+5.32	2.37 [†]	$6.12^{+6.15}_{-2.32}$	$7.48^{+1.92}_{-1.06}$	0.81 [†]	2.5^{\dagger}	<27.11	<5.57
2	316.41	386	$0.52^{+0.05}_{-0.04}$	$1.21^{+1.05}_{-0.48}$	$5.70^{+1.04}_{-0.98}$	$62.35^{+134.45}_{-36.70}$	$0.48^{+0.30}_{-0.23}$	$0.30^{+0.12}_{-0.09}$	$3.09^{+7.85}_{-1.99}$	1.84^{\dagger}	>11.10	$2.48^{+0.49}_{-0.73}$	1.12^{\dagger}	2.5^{\dagger}	< 2.40	< 0.49
3	361.95	419	$0.51^{+0.03}_{-0.03}$	$1.63^{+1.05}_{-0.88}$	$5.10^{+1.06}_{-1.13}$	$99.10^{+390.24}_{-65.90}$	$1.02^{+0.16}_{-0.24}$	$0.21^{+0.07}_{-0.04}$	$37.25^{+81.75}_{-27.66}$	2.22^{\dagger}	>6.69	$4.41^{+1.36}_{-0.58}$	0.81^{\dagger}	2.5^{\dagger}	< 1.62	< 0.33
4	375.14	391	$0.54^{+0.02}_{-0.02}$	$6.63^{+1.70}_{-4.51}$	$4.66^{+0.87}_{-0.75}$	284.31 ^{+661.94} -185.76	$0.47^{+0.25}_{-0.19}$	$0.39^{+0.12}_{-0.13}$	$2.07^{+5.41}_{-1.00}$	2.94^{\dagger}	$4.58^{+11.08}_{-1.83}$	$4.12^{+1.24}_{-0.99}$	0.96^{\dagger}	2.5^{\dagger}	< 9.67	< 1.99
5	438.13	455	$0.45^{+0.02}_{-0.02}$	$5.64^{+1.48}_{-2.54}$	$2.19^{+0.55}_{-0.78}$	$76255.50^{+600963.05}_{-75825.46}$	$0.98^{+0.18}_{-0.14}$	$0.15^{+0.03}_{-0.04}$	$203.67^{+1116.13}_{-147.11}$	1.27^{\dagger}	$5.20^{+5.60}_{-1.69}$	$4.46^{+0.70}_{-0.60}$	0.98^{\dagger}	2.5^{\dagger}	<14.13	< 2.90
6	383.75	421	$0.46^{+0.02}_{-0.02}$	$7.62^{+5.55}_{-3.23}$	$4.18^{+1.08}_{-2.26}$	587.26 ^{+5041.97}	$0.40^{+0.11}_{-0.10}$	$0.31^{+0.04}_{-0.04}$	$12.25^{+8.73}_{-4.50}$	2.13^{\dagger}	$2.70^{+1.84}_{-0.80}$	$4.01^{+1.01}_{-0.92}$	0.85^{\dagger}	2.5^{\dagger}	<12.85	< 2.64
7	392.38	408	$0.69^{+0.04}_{-0.10}$	$1.79^{+1.34}_{-1.21}$	$7.13^{+1.10}_{-0.79}$	$21.33^{+26.16}_{-10.16}$	$0.33^{+0.13}_{-0.15}$	$0.61^{+0.08}_{-0.09}$	$2.57^{+0.99}_{-0.78}$	1.63^{\dagger}	>3.53	$2.42^{+0.84}_{-0.58}$	1.23^{\dagger}	2.5^{\dagger}	_	_
8	339.51	401	$0.51^{+0.02}_{-0.02}$	$6.86^{+2.25}_{-2.25}$	$5.49^{+1.16}_{-1.25}$	$111.76^{+447.22}_{-70.08}$	$0.48^{+0.09}_{-0.11}$	$0.24^{+0.03}_{-0.02}$	$42.83^{+28.97}_{-18.15}$	0.46^{\dagger}	$4.01^{+4.96}_{-1.49}$	$2.81^{+0.61}_{-0.56}$	0.19^{\dagger}	2.5^{\dagger}	_	-
10	358.83	385	$0.73^{+0.03}_{-0.04}$	$1.83^{+0.81}_{-0.82}$	$7.58^{+0.78}_{-0.67}$	$22.39^{+13.08}_{-8.01}$	$1.45^{+0.32}_{-0.30}$	$0.22^{+0.06}_{-0.05}$	$90.14^{+317.51}_{-62.89}$	1.81^{\dagger}	$3.19^{+6.35}_{-1.26}$	$3.16^{+1.23}_{-0.58}$	1.55^{\dagger}	2.5^{\dagger}	_	_
11	400.99	447	$0.45^{+0.02}_{-0.02}$	$4.67^{+3.98}_{-2.53}$	$5.43^{+0.94}_{-1.82}$	$97.04^{+317.42}_{-52.89}$	$0.20^{+0.14}_{-0.13}$	$0.34^{+0.09}_{-0.05}$	$2.86^{+2.46}_{-1.31}$	2.13^{\dagger}	$4.55_{-1.45}^{+4.57}$	$3.80^{+0.71}_{-0.65}$	1.33^{\dagger}	2.5^{\dagger}	< 6.00	<1.23

Note. A less-than sign or greater-than sign indicates an upper limit or lower limit with 90% confidence. All errors are 90% confidence intervals. The \dagger indicates the parameter was frozen in the fit. The absorption column densities in this table are those derived from the dust maps. The units of the APEC normalization parameter (marked with *) are those that are native to the XSpec implementation: $\frac{10^{-14} \, \text{EM}}{4\pi D_A^2}$, where EM is the source emission measure and D_A is the angular diameter distance to the source.

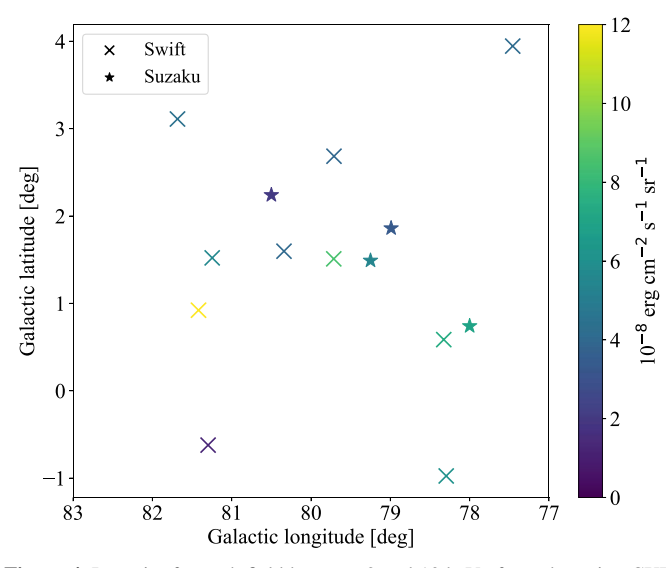


Figure 4. Intensity for each field between 2 and 10 keV after subtracting CXB compared with the position of the center of each observation. Unlike Mizuno et al. (2015), we do not find a monotonic relationship between Galactic latitude and hard X-ray emission.

3.5. Integrated Limit on the Cygnus Cocoon

In addition to the individual fits, we jointly fit the spectra from all the fields assuming that a potential X-ray signal is proportional to the integrated 1-100 TeV surface brightness, $F_{\rm X} \propto F_{\gamma}$. For the fields outside the Cocoon, $F_{\rm X}$ of the Cocoon component is set to 0. For the fields that have a nonzero HAWC flux, we tie the normalization of the Cocoon component to the Cocoon normalization in Field 1 multiplied by the ratio of the HAWC flux in each field divided by the HAWC flux in Field 1. The model adds the constraint that the GRXB and LHB temperatures are the same across all the fields within the Cocoon region. We first used the dust map based column density, and obtained the 90% confidence upper limit on the Cocoon normalization parameter to be $6.7 \times 10^{-4} \,\mathrm{cm}^{-2} \,\mathrm{s}^{-1} \,\mathrm{keV}^{-1}$. Multiplying this normalization parameter by the integrated TeV flux over the entire Cocoon (divided by the TeV flux in Field 1), we find the total flux

$$F = \int dE E \frac{dN}{dE \ dA \ dt} < 8.7 \times 10^{-11} \,\mathrm{erg} \,\mathrm{cm}^{-2} \,\mathrm{s}^{-1} \qquad (1)$$

between 2 and 10 keV when assuming $dN/dE \propto E^{-2.5}$. This limit is shown in Figure 5. Using a spectral index of 2 increased the 2–10 keV flux to 1.0×10^{-10} erg cm $^{-2}$ s $^{-1}$. The statistical significance of the likelihood ratio tests for $E^{-2.5}$ and E^{-2} were 2.3σ and 3.4σ , respectively.

We repeated the test using the column densities based on kinematic separation and calibrated on γ -ray data. We also replaced the tbabs model with tbgrain, which allows the user to set the fraction of hydrogen atoms in the molecular phase. The significance of the log-likelihood ratio test reduces to 1.6σ and 1.7σ for $E^{-2.5}$ and $E^{-2.0}$ spectra respectively. The corresponding 2–10 keV upper limits are $5.2\times10^{-11}\,\mathrm{erg}\,\mathrm{cm}^{-2}\,\mathrm{s}^{-1}$ and $4.4\times10^{-11}\,\mathrm{erg}\,\mathrm{cm}^{-2}\,\mathrm{s}^{-1}$. The results of both models are summarized in Table 3.

4. Discussion

The X-ray upper limits derived from the Swift-XRT observations constrain the electron contribution to γ -rays above 1 TeV. We adopt the leptonic model presented in Abeysekara et al. (2021), which assumes that a population of relativistic electrons following an $E^{-2.1}$ spectrum with a cutoff at 100 TeV are continuously injected by the star clusters for 3 Myr, diffuse in the Cocoon magnetic field, and inverse Compton scatter the stellar light fields and dust radiation field. When fixing the magnetic-field strength to 20 μ G, which is estimated using the gas pressure based on infrared imaging (Ackermann et al. 2011), the integrated Swift-XRT limit constrains the leptonic γ -ray emission at 1 TeV to 25% of observed emission.

Allowing a dominant leptonic contribution above 10 TeV, the X-ray observation limits the magnetic-field strength to $B \lesssim 10~\mu\text{G}$. The maximum electron energy that can be accelerated by the stellar winds in this field is $E_{e,\text{max}} \approx 34~\eta^{1/2}(B/10~\mu\text{G})^{-1/2}(\nu_w/10^3~\text{km s}^{-1})\text{TeV}$ (Blandford & Eichler 1987; Ackermann et al. 2011), where $\eta = \delta B^2/B^2$ denotes the level of magnetic-field fluctuations and $\nu_w \sim 10^3~\text{km s}^{-1}$ is the velocity of stellar winds. Even when the magnetic field in the Cocoon is as low as that in the interstellar medium ($\sim 3~\mu\text{G}$), these electrons cannot explain the photons above $\sim 62~\text{TeV}$.

Although the spectrum in Field 1 cannot rule out the purely background hypothesis, it has significantly brighter hard emission than the rest of the field. Roberts et al. (2001) searched for a X-ray counterparts to GeV sources with ASCA including GeV J2035 + 4214, which lies within the Cygnus Cocoon. Their observation of this source overlaps with Field 1 where they found three X-ray sources. One of these sources (Src1) is clearly extragalactic because it is strongly absorbed and has a spectral index of 1.41. This source was detected by Swift-XRT and excluded during data processing. The other two sources (Src2 and Src3) have absorption column densities equal to 0.98×10^{22} cm⁻² and 0.84×10^{22} cm⁻², which suggest distances consistent with the Cygnus Cocoon. These two sources have spectral indices equal to 2.02 and 2.44 and the latter is identified as an extended source. In Chandra imaging of the same region, the extended source is in fact several confused point sources (Mukherjee et al. 2003). We did not detect Src2 in Swift-XRT images. A comparison of spectra including and excluding Src3 made no apparent change in the shape of the Swift-XRT spectra.

5. Summary

We observed 11 fields in and near the Cygnus Cocoon with Swift-XRT to search for nonthermal X-ray emission. The X-ray emission for each field is well described by a background model consisting of the LHB, GRXB, and CXB. We establish upper limits for an additional power-law component for each of the fields within the Cygnus Cocoon. We also tested the hypothesis that nonthermal X-ray emission traces the TeV emission measured by HAWC and established an upper limit to this component. The limits thus obtained are sensitive to the hypotheses made to model X-ray absorption by interstellar matter, the impact of which is quantified. The X-ray upper

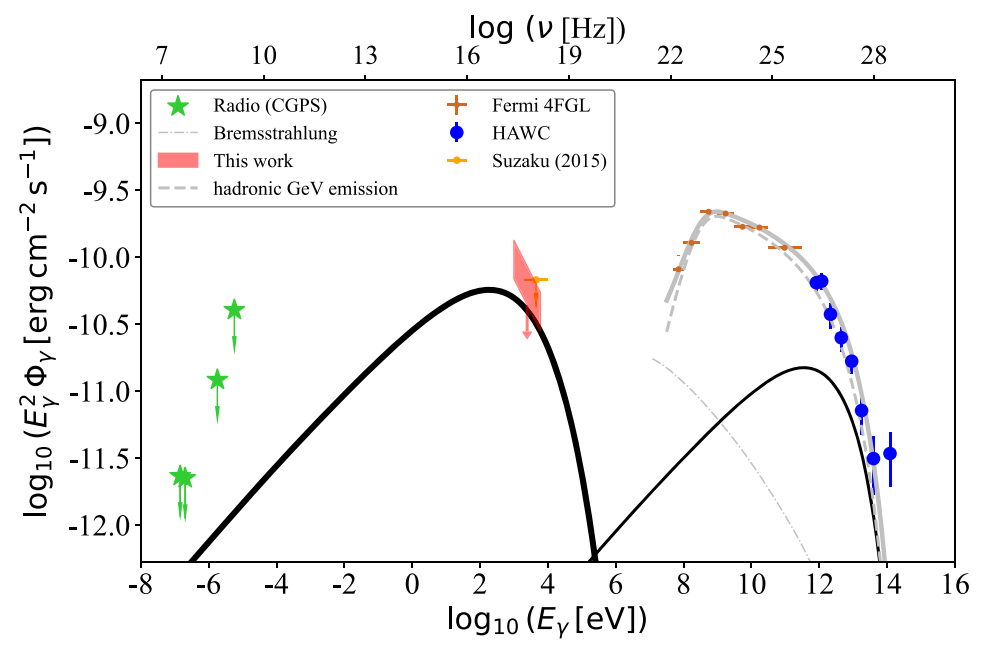


Figure 5. Multiwavelength spectral energy distribution with data and flux limits from HAWC (Abeysekara et al. 2021), Fermi-LAT (Ackermann et al. 2011), Suzaku-XIS (Mizuno et al. 2015), Swift-XRT, and CGPS (Taylor et al. 2003). The red shaded region bounds the X-ray upper limits in this work for the two hydrogen column density models considered. The black curves represent the synchrotron (thick line) and inverse Compton (thin line) emission produced by a population of electrons following an $dN_e/dE_e \propto E^{-2.1} \exp(E_e/100 \text{ TeV})$ spectrum continuously injected for 3 Myr. The kinematic separation absorption model is used. The magnetic-field strength is fixed to 20 μ G. The gray dashed—dotted curve show the Bremsstrahlung emission by these electrons. The gray dashed curve indicates the pion decay emission by protons. The gray solid curve shows the sum of the emission components. Details of the background radiation model can be found in Ackermann et al. (2011) and Abeysekara et al. (2021).

Table 3
Integrated Cocoon Likelihood Ratio Test Results and Upper Limits

C-statistic	DoF	Significance	$N_{ m H}$ Model	Cocoon Spectral Index	$\begin{array}{c} 210 \text{ keV Cocoon Flux} \\ \times 10^{-11} \text{ erg cm}^{-2} \text{ s}^{-1} \end{array}$
3946	4217	2.3σ	Dust map	2.5	<8.7
3946	4217	3.4σ	Dust map	2.0	< 10.0
3995	4217	1.6σ	Kinematic separation	2.5	< 5.2
3995	4217	1.7σ	Kinematic separation	2.0	<4.4

Note. The C-statistic is for the background-only fit. The $N_{\rm H}$ models are described in Section 3.2.

limits constrain the contribution of inverse Compton scattering to the Cocoon's TeV emission. The X-ray limits can be explained by a magnetic field below equipartition within the Cocoon or by a subdominant contribution of electrons to $\gamma\text{-rays}$ above 10 TeV. In the latter case, the inverse Compton emission can explain up to one-quarter of the TeV emission.

Acknowledgments

We thank Binita Hona for discussion on the HAWC significance map. The work of D.G. and K.F. is supported by the Office of the Vice Chancellor for Research and Graduate Education at the University of Wisconsin-Madison with funding from the Wisconsin Alumni Research Foundation. D.G. and K.F. acknowledge support from NASA (NNH20ZDA001N-Swift) and National Science Foundation (PHY-2110821). A.B. and K.L. P. acknowledge funding from the UK Space Agency.

ORCID iDs

David Guevel https://orcid.org/0000-0002-0870-2328

Andrew Beardmore https://orcid.org/0000-0001-5186-5950

Kim L. Page https://orcid.org/0000-0001-5624-2613 Ke Fang https://orcid.org/0000-0002-5387-8138 Luigi Tibaldo https://orcid.org/0000-0001-7523-570X

References

Abeysekara, A. U., Alfaro, R., Alvarez, C., et al. 2013, APh, 50, 26 Abeysekara, A. U., Albert, A., Alfaro, R., et al. 2021, NatAs, 5, 465 Ackermann, M., Ajello, M., Allafort, A., et al. 2011, Sci, 334, 1103 Ackermann, M., Ajello, M., Allafort, A., et al. 2012, A&A, 538, A71 Arnaud, K. A. 1996, in ASP Conf. Ser. 101, Astronomical Data Analysis Software and Systems V, ed. G. H. Jacoby & J. Barnes (San Francisco, CA: ASP), 17 Astiasarain, X., Tibaldo, L., Martin, P., Knödlseder, J., & Remy, Q. 2023, A&A, 671, A47 Atwood, W. B., Abdo, A. A., Ackermann, M., et al. 2009, ApJ, 697, 1071 Blandford, R., & Eichler, D. 1987, PhR, 154, 1 Cao, Z., Aharonian, F. A., An, Q., et al. 2021, Natur, 594, 33 Cash, W. 1979, ApJ, 228, 939 Ebisawa, K., Tsujimoto, M., Paizis, A., et al. 2005, ApJ, 635, 214 Foster, A., Ji, L., Smith, R., & Brickhouse, N. 2012, ApJ, 756, 128 Green, G. 2018, JOSS, 3, 695 Green, G. M., Schlafly, E., Zucker, C., Speagle, J. S., & Finkbeiner, D. 2019, Koyama, K., Makishima, K., Tanaka, Y., & Tsunemi, H. 1986, PASJ, 38, 121

```
Kuntz, K. D. 2019, A&ARv, 27, 1
Kuntz, K. D., & Snowden, S. L. 2008, ApJ, 674, 209
Liu, W., Chiao, M., Collier, M. R., et al. 2016, ApJ, 834, 33
Mattox, J. R., Bertsch, D. L., Chiang, J., et al. 1996, ApJ, 461, 396
Mizuno, T., Tanabe, T., Takahashi, H., et al. 2015, ApJ, 803, 74
Moretti, A., Campana, S., Lazzati, D., & Tagliaferri, G. 2003, ApJ,
  588, 696
Moretti, A., Pagani, C., Cusumano, G., et al. 2009, A&A, 493, 501
Morlino, G., Blasi, P., Peretti, E., & Cristofari, P. 2021, MNRAS, 504, 6096
Mukherjee, R., Halpern, J. P., Gotthelf, E. V., Eracleous, M., & Mirabal, N.
  2003, ApJ, 589, 487
NASA High Energy Astrophysics Science Archive Research Center
  (HEASARC) 2014, HEAsoft: Unified Release of FTOOLS and
   XANADU, Astrophysics Source Code Library, ascl:1408.004
Protassov, R., van Dyk, D. A., Connors, A., Kashyap, V. L., &
  Siemiginowska, A. 2002, ApJ, 571, 545
Planck Collaboration, Ade, P. A. R., Aghanim, N., et al. 2014, A&A, 571, A13
```

```
Revnivtsev, M., Sazonov, S., Gilfanov, M., Churazov, E., & Sunyaev, R. 2006,
  A&A, 452, 169
Roberts, M. S. E., Romani, R. W., & Kawai, N. 2001, ApJS, 133, 451
Smith, R. K., Brickhouse, N. S., Liedahl, D. A., & Raymond, J. C. 2001, ApJL,
  556, L91
Snowden, S. L., Collier, M. R., & Kuntz, K. D. 2004, ApJ, 610, 1182
Snowden, S. L., Egger, R., Freyberg, M. J., et al. 1997, ApJ, 485, 125
Taylor, A. R., Gibson, S. J., Peracaula, M., et al. 2003, AJ, 125, 3145
Tibet ASγ Collaboration, Amenomori, M., Bao, Y. W., et al. 2021, PhRvL,
  127, 031102
Valencic, L. A., & Smith, R. K. 2015, ApJ, 809, 66
Vieu, T., Gabici, S., Tatischeff, V., & Ravikularaman, S. 2022a, MNRAS,
  512, 1275
Vieu, T., Reville, B., & Aharonian, F. 2022b, MNRAS, 515, 2256
Wilms, J., Allen, A., & McCray, R. 2000, ApJ, 542, 914
Wright, E. L., Eisenhardt, P. R. M., Mainzer, A. K., et al. 2010, AJ,
```